



Oxygen-doped carbon nitride aerogel: A self-supported photocatalyst for solar-to-chemical energy conversion

Wenjun Jiang^a, Qiushi Ruan^b, Jijia Xie^b, Xianjie Chen^a, Yongfa Zhu^{a,*}, Junwang Tang^{b,*}

^a Department of Chemistry, Tsinghua University, Beijing, 100084, China

^b Solar Energy & Advanced Materials Research Group, Department of Chemical Engineering, UCL, Torrington Place, London, WC1E 7JE, UK



ARTICLE INFO

Keywords:

Aerogel
Oxygen-doping
Carbon nitride
Photocatalysis
Self-assembly

ABSTRACT

Herein, self-supported oxygen-doped carbon nitride aerogel (OCNA) was successfully fabricated through a facile self-assembly method combined with hydrothermal process, without adopting any harmful solvents or cross-linking agents. The fabrication mechanism of OCNA was discussed. OCNA exhibited much faster charge separation efficiency, longer carriers' lifetime than bulk carbon nitride (BCN). More importantly, oxygen-doping led to a more negative conduction band (CB) position and narrower band gap (E_g). Hence, the spectral response range of OCNA was extended dramatically and the hydrogen evolution rate (HER) of OCNA ($\lambda > 510$ nm) was about 26 times as high as that of BCN prepared herein. OCNA exhibited a remarkable apparent quantum yield (AQY) of 20.42% at 380 nm, 7.43% at 420 nm and 1.71% at 500 nm, superior to most of the reported C_3N_4 -based materials. This work paves a facile colloid chemistry strategy to assemble self-supported 3D CNA that could be widely adopted in the sustainability field.

1. Introduction

Energy and environmental issues seriously constrain the sustainable development of human society. Photocatalysis has been regarded as one of the most promising techniques to solve these problems owing to its characteristic of stable, low cost, nontoxic and efficient harvesting of solar energy [1]. To date, various photocatalytic materials have been developed from UV-driven photocatalysts represented by TiO_2 to visible-light-driven photocatalysts represented by CdS [2–10]. Unfortunately, the band structures of these inorganic semiconductors could hardly be changed restricted by their intrinsic crystal structure. Polymeric photocatalysts with delocalized conjugated π -system may be an excellent candidate to overcome these problems thanks to their tunable electronic structure. A series of conjugated polymeric photocatalysts has been developed [11–13], such as graphite carbon nitride ($g\text{-}C_3N_4$, or CN) [14–20], 1,3,5-tris-(4-ethynylphenyl)-benzene (TEPB) [21], covalent triazine frameworks [22,23], Poly(diphenylbutadiyne) (PDPB) [24], among which $g\text{-}C_3N_4$ is one of the most excellent polymeric photocatalysts thanks to the appropriate band position and facile synthetic methods [25,26].

So far, a series of strategies has been adopted to improve the photocatalytic performance of CNs, such as element doping [27–35], defect structure [27,36,37], heterostructure [38–40], copolymerization [41–43], surface modification [44,45], and so on. CNs with various

morphologies from 0D, 1D, 2D to 3D also have been designed [46–52], among which carbon nitride aerogel (CNA) or hydrogel (CNH) with 3D hierarchical structure are one of the most outstanding candidates thanks to their interconnected open-framework that could expose more reactive sites, provide convenient mass transfer channels and then promote the surface chemical reaction [46,47,53,54]. Aiming at this goal, different strategies have been presented. For instance, Yang et al. fabricated a CN aerogel with the aid of graphene [55]. Liu et al. reported a CN based hydrogel using poly(N-isopropylacrylamide) as cross-linking agents [56]. Yan et al. fabricated CN hydrogels with the aid of ionic Liquid [57]. Our group also reported the synthesis of polyaniline/CN hydrogel using polyaniline as cross-linking agents [58]. Unfortunately, all the above methods need cross-linking agents to act as supporting materials and self-supported CNA is rarely reported. Recently, Qu et al. presented a facile self-assembly method to synthesis self-supported CNA for the first time without adopting cross-linking agents [59]. This is a big breakthrough. However, the use of potassium thiocyanate as solvent may not be so eco-friendly. Therefore, a more environment-friendly method for the construction of self-supported CNA is still urgently needed.

* Corresponding authors.

E-mail addresses: zhuyf@mail.tsinghua.edu.cn (Y. Zhu), junwang.tang@ucl.ac.uk (J. Tang).

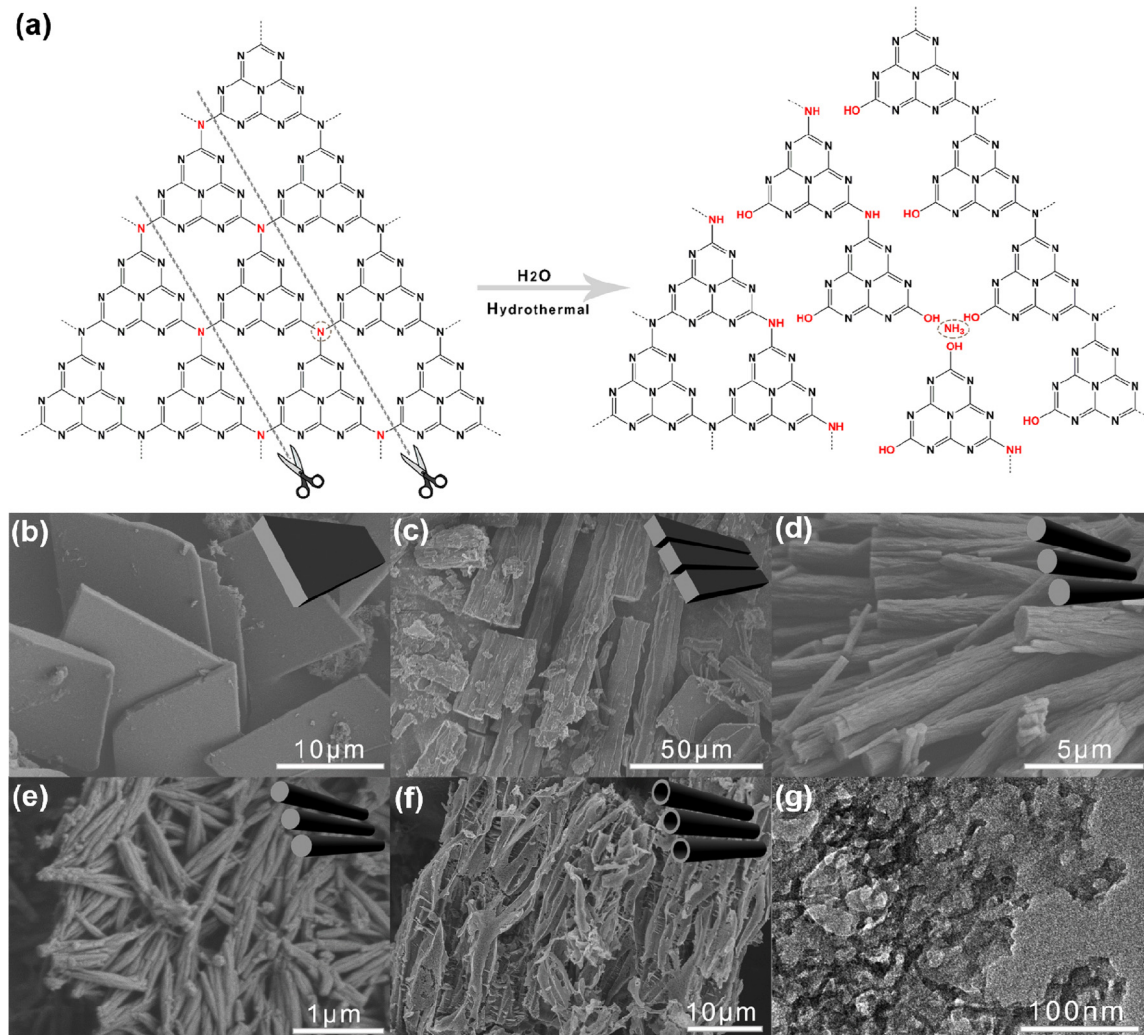


Fig. 1. (a) Scheme of the hydrothermal tailoring process. (b–e) FESEM images of CNA-3, CNA-5, CNA-6 and CNA-12. (f) FESEM image of OCNA-6. (g) TEM images of OCNA-6.

2. Results and discussions

2.1. Preparation and morphology

Here, we report the synthesis of self-supported OCNA via a facile self-assembly method combined with hydrothermal process, without adopting any harmful solvents or cross-linking agents (Scheme S1). Fig. 1a illustrates the hydrothermal tailoring process of BCN. Under high temperature and pressure, H₂O would act as a scissor tailoring the polymeric CN framework to small units. -H of H₂O was connected to the bridged tertiary nitrogen N-(C)₃ and –OH of H₂O was connected to the *sp*²-hybridized carbon (N–C = N) of the aromatic ring. As hydrothermal time increases, the degree of tailoring increases. Part of the bridged tertiary nitrogen will be converted to NH₃, which can be smelt when opening the autoclave. When hydrothermal time increases, the pH of CNH also increases (Figure S1), which indicates that there are more amino groups in the system. More hydroxyl and amino groups will be benefit for the dispersion of the samples. The Tyndall effect could be observed when the red laser passes the transparent sol solution (Figure S1), which demonstrates the formation of sol solution. Cotton-like ultra-light white aerogel with higher specific surface area could be obtained when the as-prepared CNH was directly dehydrated via a freeze-drying process (Figure S1 and S2). Fig. 1b–e shows the FESEM images of CNA with different hydrothermal time. When the hydrothermal time is 3 h, the morphology of CNA is large sheet with regular geometry and the

sheet thickness is in the micron level. When hydrothermal time is extended to five hours, both large sheet and rod-like structure could be observed and the surface of the sample is rougher. It can be speculated that the rod-like structure is formed by the breakage of the sheet-like structure. When hydrothermal time is extended to six hours, the morphology of CNA is structured trunk-shaped rod and the diameter is 1–3 μm. In order to investigate the detailed morphology, we furtherly observed the TEM of CNA-6 (Figure S3). It can be seen that the trunk-shaped rod is composed of nanofibers with a diameter of about 30 nm. Further extending the hydrothermal time to 12 h, the morphology of CNA is still structured trunk-shaped rod but with smaller diameter (0.3–0.5 μm). When calcining the CNA under N₂ atmosphere, CNA will re-polymerize into OCNA and the color of white aerogel turns back to yellow (Figure S1). As shown in Fig. 1f, OCNA-6 exhibits a 3D hierarchical structure. Firstly, the hollow tubular structure makes up the 3D framework of the aerogel (Figure S4). Then, the hollow tubular structure is composed of dendritic nanofibers (Fig. 1g). It can be speculated that the hollow tubular structure is the result of the re-polymerization of trunk-shaped rod in the calcining process since the volume will shrink during the process of dehydration condensation, which will be discussed later.

2.2. Fabrication mechanism of OCNA

To further investigate the formation processes of the aerogels, the

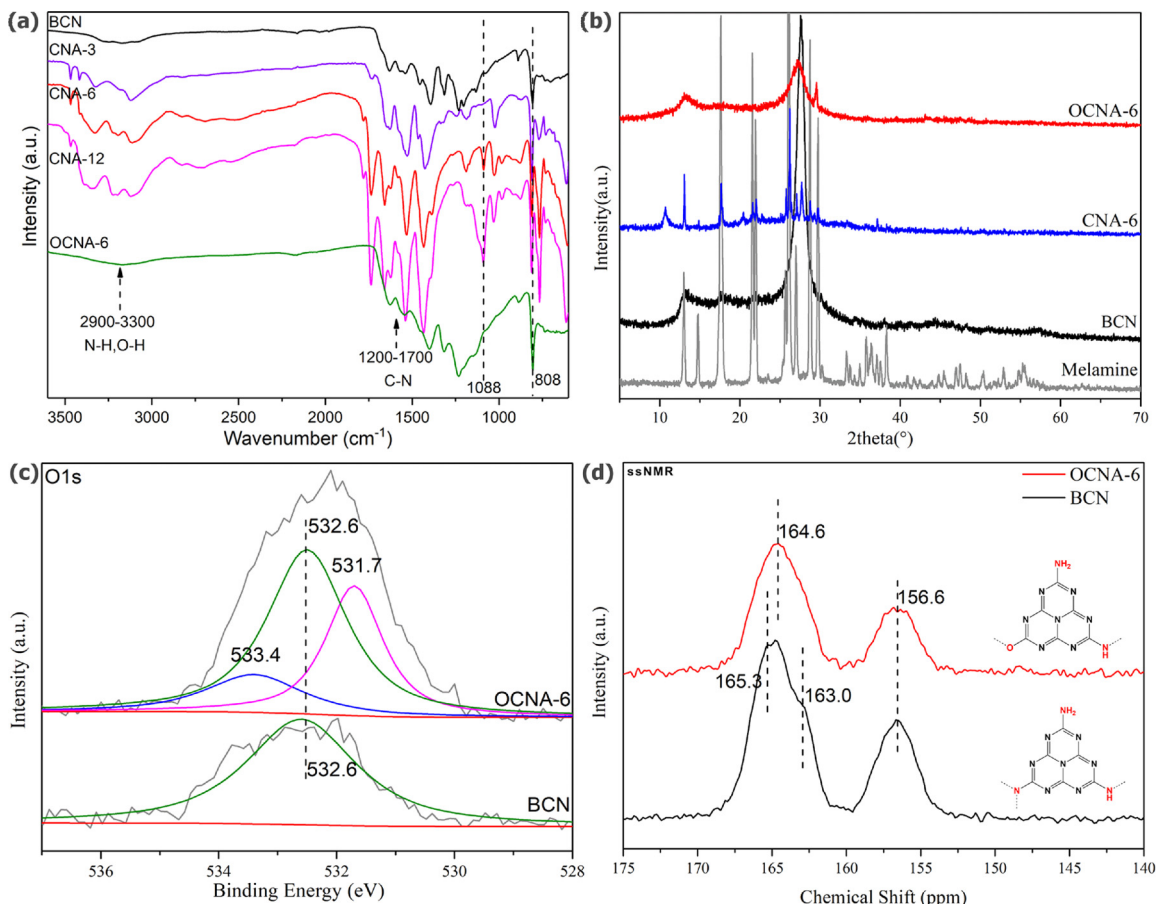
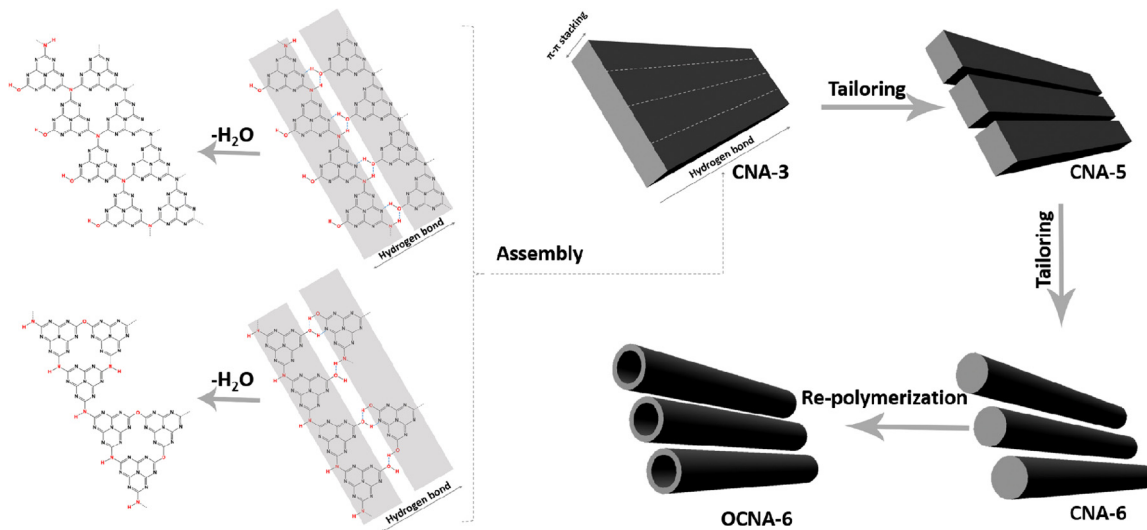


Fig. 2. (a) FT-IR spectra and (b) XRD patterns of different samples. (c) XPS and (d) solid-state ^{13}C NMR spectra of BCN and OCNA-6.



Scheme 1. Scheme of the fabrication process of OCNA.

samples was characterized via FT-IR spectroscopy (Fig. 2a). The peak at about 808 cm^{-1} represents the representative breathing mode of the CN heterocycles [58]. The peaks at $1200\text{--}1700\text{ cm}^{-1}$ represent the characteristic stretching vibration modes of the CN heterocycles [59]. The wide peaks in the region of $2900\text{--}3300\text{ cm}^{-1}$ represent the N-H and O-H stretching vibration [59]. Compared with the BCN, the peaks of CNA at this region exhibit stronger intensity demonstrating that there are more hydroxyl and amino groups, which indicates that the condensation was decreased [60]. A new peak at 1088 cm^{-1} was observed

for CNA, which represents the C-O stretching vibration. When hydrothermal time increases, the intensity of the peak at 1088 cm^{-1} also increases indicating that there will be more hydrogen bonds between N-H and O-H. The hydrogen-bond interaction is quite important in the self-assembly process of CNA. The XRD pattern of CNA-6 is quite similar with that of melamine (Fig. 2b), indicating that the BCN was tailored into melamine-based small molecular and the CNA was fabricated through the self-assembly of these small molecular. Scheme 1 illustrates the two possible self-assembly mechanism of CNA. The

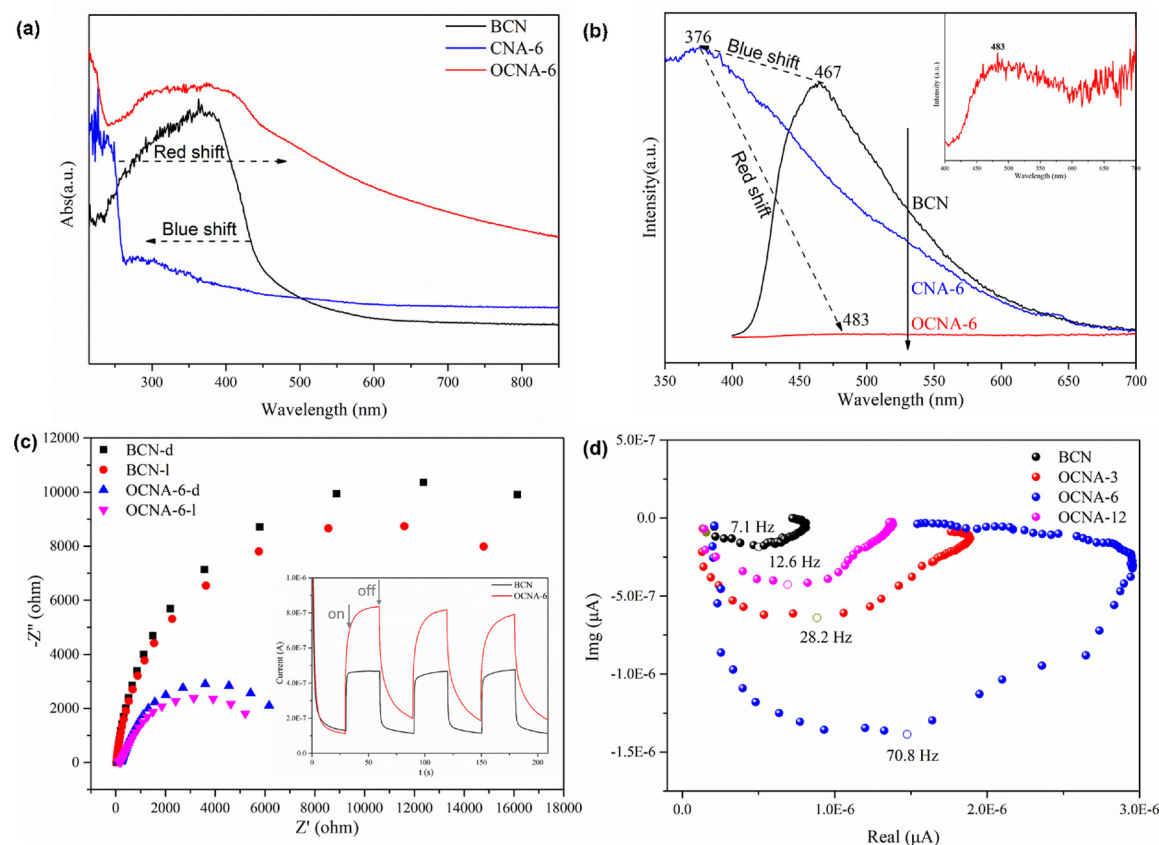


Fig. 3. (a) DRS and (b) PL spectra of BCN, CNA-6 and OCNA-6 (insert: enlarged PL plot of OCNA-6). (c) photocurrent responses of BCN and OCNA-6 (insert: EIS Nyquist plots). (d) IMPS spectra of different samples at 0.8 V_{Ag/AgCl}.

hydrogen bonds may exist either between N–H and O–H or between O–H and O–H. In one direction parallel to the scheme, the intermolecular hydrogen bonding drives the self-assembly of the layers. In the direction perpendicular to the scheme, π - π interaction conducts the stacking of the layers. Fig. 2b shows the XRD pattern, peak at 13.1° represents the (100) interplanar heptazine packing ($d = 0.68$ nm) and peak at 27.5° represents the (002) interlayer π - π stacking ($d = 0.33$ nm) [61]. Interestingly, a new peak for OCNA-6 was observed at 29.5° and the corresponding lattice plane spacing is 0.30 nm (Figure S4c). The new peak could be ascribed to the reduced interlayer π - π stacking and the reduced interlayer π - π stacking distance could promote the charge transfer between the layers and from the bulk to the interface [61]. When the hydrothermal time is 3 h, the morphology of CNA is large sheet with regular geometry. As the hydrothermal time increases, in another direction parallel to the scheme, part of the bridged tertiary nitrogen will be further cut off and the size of the sheet will get smaller. As the hydrothermal time is further extended, the sheet with smaller size will be converted to trunk-shaped rod. At last, the trunk-shaped rod will be converted to hollow tubular structure in the calcining process.

To further investigate the re-polymerization processes, the samples was characterized via XPS and solid-state ^{13}C NMR spectroscopy (Fig. 2c and d). As shown in Fig. 2c, the peak at 532.6 eV is attributed to the adsorbed H_2O [58]. Interestingly, two new peaks are found at 533.4 eV and 531.7 eV for OCNA-6 that represent C–O–C and C–OH, respectively [29]. Therefore, we can speculate that oxygen-doping was introduced during the re-polymerization. Scheme 1 illustrates the detailed formation process of oxygen-doping. H_2O will be removed in the hydrogen bonds between two molecular under high temperature. Then the bridged tertiary nitrogen will be replaced by oxygen and oxygen-doping is introduced. In the C1s spectra (Figure S5a and S5c), three peaks at 284.8 eV, 286.4 eV and 288.3 eV could be observed. The peak

at 284.8 eV is attributed to the carbon contaminations. Peak at 288.3 eV represents N = C–N and peak at 286.4 eV is assigned to C–O [29]. Compared with BCN, the area ratio of the peak at 286.4 eV for OCNA-6 is much larger, indicating that the oxygen content of OCNA-6 is higher. In the N1s spectra (Figure S5b and S5d), three peaks are observed at 404.6 eV, 400.9 eV and 398.8 eV, which are assigned to the positive charge localization effect, N–(C)₃ or –NH_x and C = N–C, respectively [58]. Compared with BCN, the area ratio of the peak at 400.9 eV for OCNA-6 is much smaller, demonstrating that the bridged tertiary nitrogen content of OCNA-6 is decreased and part of the bridged tertiary nitrogen is replaced by oxygen. The atomic concentration of different samples is investigated via XPS in Table S1. Compare with BCN, the OCNA exhibits higher O and lower N concentration, demonstrating that oxygen-doping was successfully introduced. Interestingly, the degree of oxygen doping can be adjusted by hydrothermal time. As the hydrothermal time increases, the degree of oxygen doping also increases. Raman peak at 700 cm⁻¹ represents the in-plane bending vibrations of the N–(C)₃ linked to heptazine units (Figure S6) [29]. The peak of OCNA-6 at 700 cm⁻¹ shows a red shift compared to BCN, which is also a supporting evidence of oxygen-doping. Solid-state ^{13}C NMR was also adopted to prove the presence of oxygen doping (Fig. 2d). The peak at 156.6 ppm represents the C atom in CN₃ [36], which could be observed in both BCN and OCNA-6 demonstrating that the basic heptazine was not destroyed during the hydrothermal treatment. For BCN, the peaks at 163.0 ppm and 165.3 ppm are assigned to the C atom in CN₂(NH) and CN₂(NH₂), respectively [29]. However, for OCNA-6, a new peak at 164.6 ppm could be observed representing the C atom CN₂(O) [29], which is a conclusive evidence for the oxygen doping. Furthermore, it could be found that the peaks of BCN are broadened compared with OCNA-6, indicating that the structural disorder is increased. The increased structural disorder may be helpful for the band structure

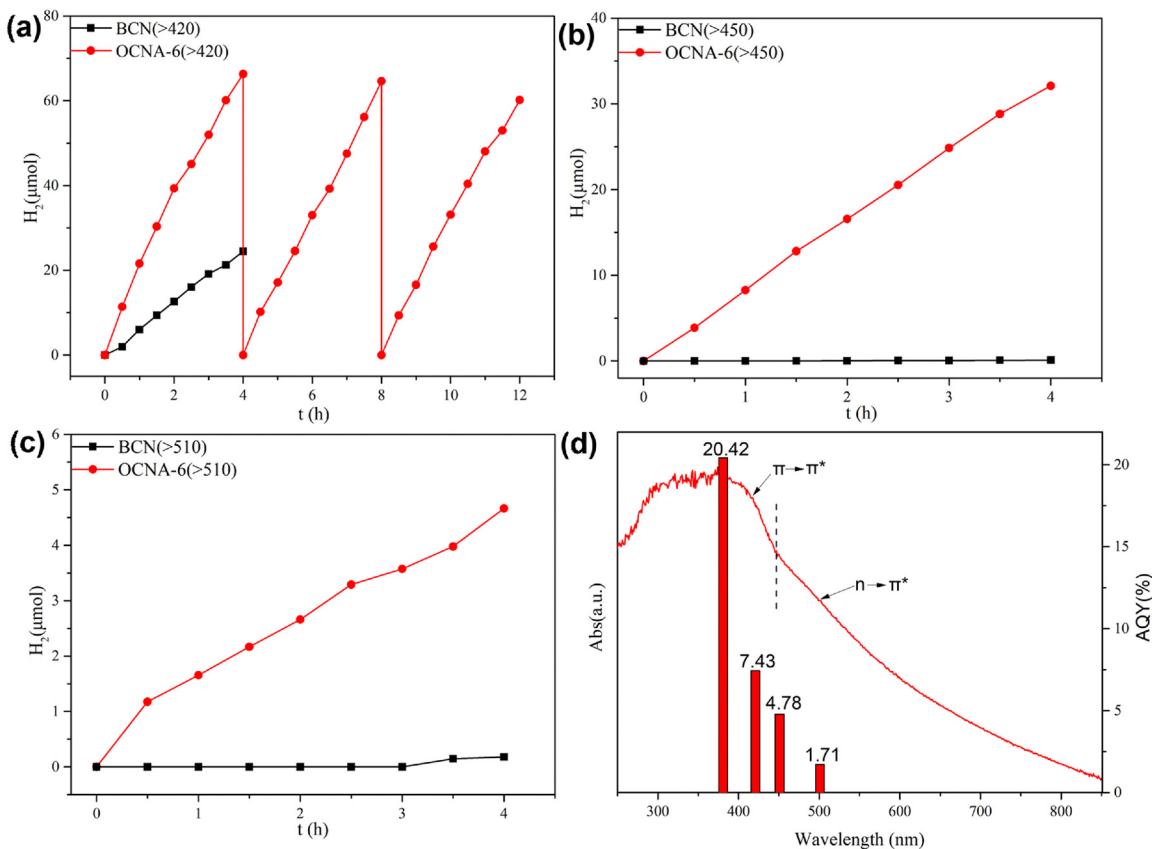


Fig. 4. HER of BCN and OCNA-6 (a) $\lambda > 420$ nm, (b) $\lambda > 450$ nm and (c) $\lambda > 510$ nm. (d) wavelength-dependent AQY (right axis) and DRS (left axis) of OCNA-6.

adjustment and the separation and transfer of photoinduced carriers.

2.3. Structure-reactivity relationship

To verify this point of view, the UV-vis spectra were tested (Fig. 3a). Compared with BCN, the absorption edge (λ_g) of CNA-6 exhibits a strong blue shift, which could be attributed to the quantum size effect since BCN was tailored to smaller molecular [62–64]. After the re-polymerization, the absorption edge of OCNA-6 shows a strong red shift, indicating that the band gap narrows greatly. More importantly, the absorption intensity increases dramatically in both UV and Vis region, indicating that the light harvesting performance is promoted greatly. The enhanced light harvesting can be attributed to the 3D network structure, since the interconnected framework could increase the multireflection of the sun light [46]. The flat-band potential and the band gap (Eg) can be evaluated by the Mott–Schottky plots and Tauc lots (Figure S7). The flat-band potential could be adopted to approximately evaluate the CB of n-type semiconductor [42,65,66]. Combine the values of CB and Eg, the valence band (VB) value will be determined. The band structure alignments are shown in Figure S7f and Table S2. The CB of OCNA-6 is more negative than that of BCN, indicating that OCNA-6 may show a stronger reduction ability for photoinduced electrons. The VB of OCNA-6 is less positive than that of BCN, which also could be confirmed by the XPS valence band spectra (Figure S7e). Both the position of CB and VB for OCNA-6 are eligible for the photocatalytic hydrogen or oxygen evolution [67].

The photoluminescence (PL) spectra exhibits the similar phenomenon with the UV-Vis spectra. As shown in Fig. 3b, BCN exhibits a sharp peak at about 467 nm. The peak of CNA-6 shows an obvious blue shift to 376 nm and the PL intensity is much stronger, which indicates that the photoinduced electrons and holes recombine more easily and goes against the photocatalytic reaction [28,61,68,69]. After the re-polymerization, the PL peak of OCNA-6 shifts back to about 483 nm and

the PL intensity is extremely weak, demonstrating that the electron-hole recombination rate for OCNA-6 is much lower than that of BCN [28,61,68,69]. To further verify this point of view, the time-resolved PL was conducted (Figure S8). The emission peaks determine the mean radiative lifetimes (τ) of the photoinduced carriers (Table S3). The PL lifetime reflects the time for photoinduced carriers to decay to their “1/e” by radiative recombination. Hence, longer PL lifetime represents slower charge recombination [70,71]. The τ for BCN and OCNA-6 is 8.715 ns and 13.365 ns, respectively. The remarkable prolonged PL lifetime for OCNA-6 indicates that the charge recombination is retarded and charge transfer is more efficient. Furthermore, the enhanced charge transport could be confirmed by the reduced hemicycle radius in the electrochemical impedance spectra (EIS, Fig. 3c), since the reduced hemicycle radius reflects smaller electric resistance [31,61]. The photocurrent response for OCNA-6 is approximately 1.8 times as high as that of BCN, proving that the transfer of the photoinduced carriers is promoted (insert of Fig. 3c). Interestingly, when the light is off, the photocurrent of BCN decreases to zero quickly while the photocurrent of OCNA-6 exhibits an obvious delay, indicating that recombination of photoinduced carriers is hindered and the lifetime is prolonged greatly. Intensity modulated photocurrent spectroscopy (IMPS) is used to evaluate the charge transport performance (Fig. 3d). The transit time (τ_D) could be obtained by $\tau_D = (2\pi f_{\max})^{-1}$, which represents the average time photoinduced electrons need to reach the back contact [72,73]. f_{\max} is the frequency where the minimum in the IMPS plot occurs. The f_{\max} and τ_D of different samples are listed in Table S4. The τ_D of BCN is 22.4 ms while τ_D of OCNA-6 is only 2.2 ms, demonstrating that OCNA-6 possesses a much faster electron transfer rate and thus promotes the photocurrent density.

2.4. Photocatalytic hydrogen performance

It is reasonable to speculate that the OCNA will exhibit an excellent

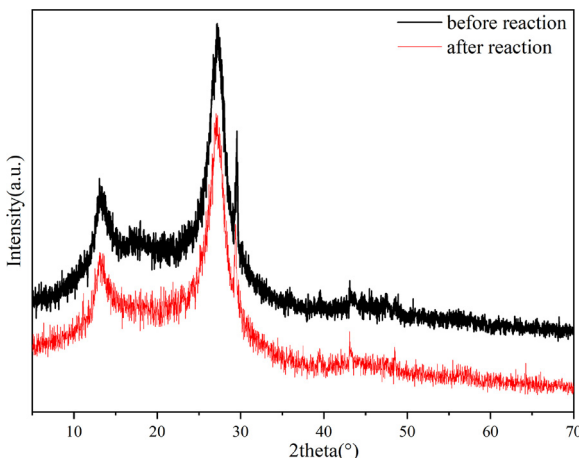


Fig. 5. XRD patters of OCNA-6 before and after photocatalytic reaction.

HER performance thanks to the appropriate band location and outstanding charge separation and migration efficiency. With the increase of the re-polymerization temperature, the HER is also increasing (Figure S9). However, when the temperature over 550 °C, the sample will be carbonized. As shown in Fig. 4a, the HER of OCNA-6 (16.57 μmol/h) is about 3 times as high as that of BCN (6.12 μmol/h) when $\lambda > 420$ nm. Cyclic experiments were carried on to test the stability of OCNA-6 under the same conditions. The HER showed a decay of about 9.2% after three cycles. The decay may be ascribed to the decrease of the sacrificial agent since no additional sacrificial agent was added to the reacrion system. The XRD (Fig. 5) further demonstrates the stability of OCNA-6. The FI-IR and XRD patterns of OCNA-6 before and after the irradiation in the absence of solvents also showed no obvious differences (Figure S10), demonstrating the stability of OCNA-6. When changing the wavelength ($\lambda > 450$ nm, Fig. 4b), the HER of OCNA-6 (8.02 μmol/h) is about 8 times as high as that of BCN (1.01 μmol/h). Further extending the wavelength ($\lambda > 510$ nm, Fig. 4c), the HER of OCNA-6 (1.17 μmol/h) is about 26 times as high as that of BCN (0.045 μmol/h). BCN showed no hydrogen evolution in the first three hours. This is because the hydrogen concentration in the first three hours was lower than the detection limits of GC. The longer the wavelength, the more obvious the difference in performance is (Figure S11). Therefore, it can be concluded that the spectral response range of OCNA was extended dramatically. The absorption band less than 445 nm is ascribed to the general $\pi \rightarrow \pi^*$ electron transition of the conjugated system while the new absorption band more than 445 nm is attributed to the $n \rightarrow \pi^*$ electron transition of the lone pairs in the edge N atoms (Fig. 4d) [61]. The $n \rightarrow \pi^*$ electron transition is beneficial for the utilization of visible light with longer wavelengths. Fig. 4d exhibits the apparent quantum yield (AQY) of OCNA-6, which is well matched with the DRS. The AQY is 20.42% (380 nm), 7.43% (420 nm), 4.78% (450 nm) and 1.71% (500 nm). To the best of our knowledge, although the AQY of OCNA at 420 nm is the not the highest, the AQY of OCNA at 450 nm is still 4.78%, which is superior to most of the reported carbon nitride materials (Table S5) [28,29,59,61,74,75].

3. Conclusion

The enhanced photocatalytic performance owes to the following reasons: Firstly, the interconnected open-framework of the self-supported aerogels could expose more reactive sites, provide convenient mass transfer channels and then promote the surface chemical reaction. Secondly, oxygen-doping adjusts the band structure of carbon nitride, resulting in a more negative CB and extended spectral response range. More importantly, oxygen-doping facilitates the charge separation and migration efficiency and prolongs the lifetime of photoinduced carriers, resulting in a higher H₂ evolution rate. In summary, we successfully

fabricate self-supported oxygen-doped carbon nitride aerogel via a facile self-assembly method combined with hydrothermal process, without adopting any harmful solvents or cross-linking agents. This eco-friendly method paves a facile colloid chemistry strategy to assemble self-supported 3D CNA that could be widely adopted in the sustainability field.

4. Experimental section

4.1. Materials preparation

Synthesis of BCN: BCN was synthesized by heating the mixture of dicyandiamide and thiourea in air (in a four-to-one molar ratio) as follows: 30–300 °C (temperature rate 8 °C/min); 300–500 °C (temperature rate 2 °C/min); 500–550 °C (temperature rate 1 °C/min); then kept at 550 °C for 4 h.

Synthesis of CNH: 0.5 g BCN was dispersed into 20 mL deionized water. Then transfer it into a 100 mL Teflon-lined reactor and kept at 210 °C for a certain time to obtain a suspension (3 h for CNH-3, 5 h for CNH-5, etc.).

Synthesis of CNA: The as-prepared CNH was directly dehydrated via a freeze-drying process. Cotton-like aerogel was obtained labelled as CNA (CNH-3 corresponds to CNA-3, CNH-5 corresponds to CNA-5, etc.).

Synthesis of OCNA: A certain quality of CNA was placed in a crucible and be calcined in N₂ atmosphere. 30–500 °C (temperature rate 8 °C/min); 500–550 °C (temperature rate 1 °C/min); then kept at 550 °C for 4 h. At last, oxygen-doped carbon nitride labelled as OCNA will be obtained (CNA-3 corresponds to OCNA-3, CNH-5 corresponds to OCNA-5, etc.).

4.2. Characterization

FESEM images were obtained by Field Emission Scanning Electron Microscopy (Hitachi SU-8010). TEM images and HRTEM images were gotten via transmission electron microscope (Hitachi HT 7700) and field emission transmission electron microscope (JEM 2100 F), respectively. DRS was obtained through UV-vis spectrophotometer (Hitachi UV-3010). XRD patterns were gotten via X-ray diffractometer (Bruker D8 Advance, $\lambda = 0.154$ nm). Roman spectra were recorded by Raman spectrometer (HORIBA HR800, excitation laser: 325 nm). FT-IR spectra were recorded by infrared spectrometer (Bruker V70). XPS spectra were recorded by PHI Quantera SXM™ system. ¹³C solid-state nuclear magnetic resonance (NMR) spectra were recorded by JNM-ECZ600R/M. PL spectra were recorded by fluorescence spectrometer (JASCO FP-6500, $\lambda_{ex} = 318$ nm). Time-resolved PL test was carried on an Edinburgh Instruments F9000 ($\lambda_{ex} = 405$ nm, $\lambda_{em} = 467$ nm).

4.3. Photocatalytic tests

The photocatalytic hydrogen performances were tested through the Perfect Light agitated reactor (LabSolar-6 A). A 300 W Xenon lamp equipped with cut-off filter (420, 450 or 510 nm) was used as the visible-light source. The water filter was used to avoid the heat effects (water temperature: 4 °C). Every 30 min, a specified volume of gas was taken from the system and then analyzed by gas chromatograph (GC-7800). 25 mg photocatalyst was added into 100 mL solution containing 10 mL TEOA as sacrificial agent. 3 wt.% Pt as the cocatalyst was in-situ photodeposited on the surface of photocatalysts.

The apparent quantum yield (AQY) at various monochromatic lights (380 nm, 420 nm, 450 nm, 500 nm) were measured in the aid of different band-pass filters. The irradiation area was $1/4\pi 1.8 \times 1.8$ cm⁻², controlled by a light shield. For the AQY measurement, 50 mg photocatalyst was used. The AQY at different monochromatic wavelength light was obtained through the equation:

$$\text{AQY} = \frac{Ne}{Np} \times 100\% = \frac{2 \times M \times N_A \times h \times c}{S \times P \times t \times \lambda} \times 100\%$$

Np: incident photons, Ne: the amount of reaction electrons, S: irradiation area, P: irradiation intensity, t: reaction time, λ : wavelength of the monochromatic light, M: the amount of H₂, N_A: The Avogadro constant, h: The Plank constant, c: light speed.

4.4. Photoelectrochemical tests

The photoelectrochemical experiments except IMPS were tested via a three-electrode electrochemical system using 0.1 M Na₂SO₄ as electrolyte solution (CHI-660D, China). Saturated calomel electrode and Pt wire served as reference electrode and counter electrode.

The IMPS test was investigated via an electrochemical analyzer using 0.1 M Na₂SO₄ as electrolyte solution (IVIUM Technologies). An Ag/AgCl electrode and a Pt net served as the reference and counter electrodes.

Acknowledgements

This work was partly supported by National Natural Science Foundation of China (21437003, 21761142017, 21673126, 21621003), Tsinghua Fudaoyuan Research Foundation and Collaborative Innovation Center for Regional Environmental Quality. Q.R. thanks the support of the China Scholarship Council. J.T. thanks the funding from EPSRC grant (EP/N009533/1).

Appendix A. Supplementary data

Supplementary material related to this article can be found, in the online version, at doi:<https://doi.org/10.1016/j.apcatb.2018.05.050>.

References

- [1] Q. Wang, T. Hisatomi, Q. Jia, H. Tokudome, M. Zhong, C. Wang, Z. Pan, T. Takata, M. Nakabayashi, N. Shibata, Scalable water splitting on particulate photocatalyst sheets with a solar-to-hydrogen energy conversion efficiency exceeding 1%, *Nat. Mater.* 15 (2016) 611–615.
- [2] B. Qiu, M. Xing, J. Zhang, Mesoporous TiO₂ nanocrystals grown *in situ* on graphene aerogels for high photocatalysis and lithium-ion batteries, *J. Am. Chem. Soc.* 136 (2014) 5852–5855.
- [3] Y. Xu, Y. Ye, T. Liu, X. Wang, B. Zhang, M. Wang, H. Han, C. Li, Unraveling a single-step simultaneous two-electron transfer process from semiconductor to molecular catalyst in a CoPy/CdS hybrid system for photocatalytic H₂ evolution under strong alkaline conditions, *J. Am. Chem. Soc.* 138 (2016) 10726–10729.
- [4] K.K. Sakimoto, A.B. Wong, P. Yang, Self-photosensitization of nonphotosynthetic bacteria for solar-to-chemical production, *Science* 351 (2016) 74–77.
- [5] H. Hirakawa, M. Hashimoto, Y. Shiraishi, T. Hirai, Photocatalytic conversion of nitrogen to ammonia with water on surface oxygen vacancies of titanium dioxide, *J. Am. Chem. Soc.* 139 (2017) 10929–10936.
- [6] Q. Li, X. Li, S. Wageh, A.A. Al-Ghamdi, J. Yu, CdS/Graphene nanocomposite photocatalysts, *Adv. Energy Mater.* 5 (2015) 1500010.
- [7] Y. Zhou, Q. Yi, M. Xing, L. Shang, T. Zhang, J. Zhang, Graphene modified mesoporous titania single crystals with controlled and selective photoredox surfaces, *Chem. Commun.* 52 (2016) 1689–1692.
- [8] K. Mori, K. Miyawaki, H. Yamashita, Ru and Ru–Ni nanoparticles on TiO₂ support as extremely active catalysts for hydrogen production from ammonia–borane, *ACS Catal.* 6 (2016) 3128–3135.
- [9] L. Wu, F. Li, Y. Xu, J.W. Zhang, G. Li, H. Li, Plasmon-induced photoelectrocatalytic activity of Au nanoparticles enhanced TiO₂ nanotube arrays electrodes for environmental remediation, *Appl. Catal. B: Environ.* 164 (2015) 217–224.
- [10] Y. Deng, M. Xing, J. Zhang, An advanced TiO₂/Fe₂TiO₅/Fe₂O₃ triple-heterojunction with enhanced and stable visible-light-driven fenton reaction for the removal of organic pollutants, *Appl. Catal. B: Environ.* 211 (2017) 157–166.
- [11] G. Zhang, Z.A. Lan, X. Wang, Conjugated polymers: catalysts for photocatalytic hydrogen evolution, *Angew. Chem. Int. Ed.* 55 (2016) 15712–15727.
- [12] M.Z. Rahman, P.C. Tapping, T.W. Kee, R. Smernik, N. Spooner, J. Moffatt, Y. Tang, K. Davey, S.Z. Qiao, A. Benchmark, Quantum yield for water photoreduction on amorphous carbon nitride, *Adv. Funct. Mater.* 27 (2017) 1702384.
- [13] D.J. Woods, R.S. Sprick, C.L. Smith, A.J. Cowan, A.I. Cooper, A solution-processable polymer photocatalyst for hydrogen evolution from water, *Adv. Energy Mater.* 7 (2017) 1700479.
- [14] R. Godin, Y. Wang, M.A. Zwijnenburg, J. Tang, J.R. Durrant, Time-resolved spectroscopic investigation of charge trapping in carbon nitrides photocatalysts for hydrogen generation, *J. Am. Chem. Soc.* 139 (2017) 5216–5224.
- [15] V.W.H. Lau, D. Klose, H. Kasap, F. Podjaski, M.C. Pignié, E. Reisner, G. Jeschke, B.V. Lotsch, Dark photocatalysis: storage of solar energy in carbon nitride for time-delayed hydrogen generation, *Angew. Chem. Int. Ed.* 56 (2017) 510–514.
- [16] J. Liu, S. Xie, Z. Geng, K. Huang, L. Fan, W. Zhou, L. Qiu, D. Gao, L. Ji, L. Duan, Carbon nitride supramolecular hybrid material enabled high-efficiency photocatalytic water treatments, *Nano Lett.* 16 (2016) 6568–6575.
- [17] P. Yang, H. Ou, Y. Fang, X. Wang, A facile steam reforming strategy to delaminate layered carbon nitride semiconductors for photoredox catalysis, *Angew. Chem.* 129 (2017) 4050–4054.
- [18] M. Zhu, S. Kim, L. Mao, M. Fujitsuka, J. Zhang, X. Wang, T. Majima, Metal-free photocatalyst for H₂ evolution in visible to near-infrared region: black phosphorus/graphitic carbon nitride, *J. Am. Chem. Soc.* 139 (2017) 13234–13242.
- [19] W. Che, W. Cheng, T. Yao, F. Tang, W. Liu, H. Su, Y. Huang, Q. Liu, J. Liu, F. Hu, Fast photoelectron transfer in (Cring)-C₃N₄ plane heterostructural nanosheets for overall water splitting, *J. Am. Chem. Soc.* 139 (2017) 3021–3026.
- [20] S. Zhao, X. Zhao, H. Zhang, J. Li, Y. Zhu, Covalent combination of polyoxometalate and graphitic carbon nitride for light-driven hydrogen peroxide production, *Nano Energy* 35 (2017) 405–414.
- [21] L. Wang, Y. Wan, Y. Ding, S. Wu, Y. Zhang, X. Zhang, G. Zhang, Y. Xiong, X. Wu, J. Yang, Conjugated microporous polymer nanosheets for overall water splitting using visible light, *Adv. Mater.* 29 (2017) 1702428.
- [22] P. Kuhn, M. Antonietti, A. Thomas, Porous, covalent triazine-based frameworks prepared by ionothermal synthesis, *Angew. Chem.* 47 (2008) 3450.
- [23] K. Schwinghammer, S. Hug, M. Mesch, J. Senker, B.V. Lotsch, Phenyl-triazine oligomers for light-driven hydrogen evolution, *Energy Environ. Sci.* 8 (2015) 3345–3353.
- [24] S. Ghosh, N.A. Kouamé, L. Ramos, S. Remita, A. Dazzi, A. Deniset-Besseau, P. Beaunier, F. Goubard, P.-H. Aubert, H. Remita, Conducting polymer nanostructures for photocatalysis under visible light, *Nat. Mater.* 14 (2015) 505–511.
- [25] J. Fu, J. Yu, C. Jiang, B. Cheng, g-C₃N₄-based heterostructured photocatalysts, *Adv. Energy Mater.* 8 (2018) 1701503.
- [26] G. Liu, T. Wang, H. Zhang, X. Meng, D. Hao, K. Chang, P. Li, T. Kako, J. Ye, Nature-inspired environmental “Phosphorylation” boosts photocatalytic H₂ production over carbon nitride nanosheets under visible-light irradiation, *Angew. Chem.* 127 (2015) 13765–13769.
- [27] H. Yu, R. Shi, Y. Zhao, T. Bian, Y. Zhao, C. Zhou, G.I.N. Waterhouse, L.-Z. Wu, C.-H. Tung, T. Zhang, Alkali-assisted synthesis of nitrogen deficient graphitic carbon nitride with tunable band structures for efficient visible-light-driven hydrogen evolution, *Adv. Mater.* 29 (2017) 1605148.
- [28] S. Guo, Z. Deng, M. Li, B. Jiang, C. Tian, Q. Pan, H. Fu, Phosphorus-doped carbon nitride tubes with a layered micro-nanostructure for enhanced visible-light photocatalytic hydrogen evolution, *Angew. Chem. Int. Ed.* 55 (2016) 1830–1834.
- [29] Y. Wang, M.K. Bayazit, S. Moniz, Q. Ruan, C.C. Lau, N. Martsinovich, J. Tang, Linker-controlled polymeric photocatalyst for highly efficient hydrogen evolution from Water, *Energy Environ. Sci.* 10 (2017) 1643–1651.
- [30] K. Wang, Q. Li, B. Liu, B. Cheng, W. Ho, J. Yu, Sulfur-doped g-C₃N₄ with enhanced photocatalytic CO₂-reduction performance, *Appl. Catal. B: Environ.* 176 (2015) 44–52.
- [31] J. Xu, S. Cao, T. Brenner, X. Yang, J. Yu, M. Antonietti, M. Shalom, Supramolecular chemistry in molten sulfur: preorganization effects leading to marked enhancement of carbon nitride photoelectrochemistry, *Adv. Funct. Mater.* 25 (2015) 6265–6271.
- [32] F. Liu, J. Yu, G. Tu, L. Qu, J. Xiao, Y. Liu, L. Wang, J. Lei, J. Zhang, Carbon nitride coupled Ti-SBA15 catalyst for visible-light-driven photocatalytic reduction of Cr (VI) and the synergistic oxidation of phenol, *Appl. Catal. B: Environ.* 201 (2017) 1–11.
- [33] Y. Wu, M. Wen, M. Navlani-García, Y. Kuwahara, K. Mori, H. Yamashita, Palladium nanoparticles supported on titanium-doped graphitic carbon nitride for formic acid dehydrogenation, *Chem.-Asian J.* 12 (2017) 860–867.
- [34] Z. Lin, X. Wang, Nanostructure engineering and doping of conjugated carbon nitride semiconductors for hydrogen photosynthesis, *Angew. Chem. Int. Ed.* 52 (2013) 1735–1738.
- [35] X. Wang, X. Chen, A. Thomas, X. Fu, M. Antonietti, Metal-containing carbon nitride compounds: a new functional organic-metal hybrid material, *Adv. Mater.* 21 (2009) 1609–1612.
- [36] V.W.-H. Lau, I. Moudrakovski, T. Botari, S. Weinberger, M.B. Mesch, V. Duppel, J. Senker, V. Blum, B.V. Lotsch, Rational design of carbon nitride photocatalysts by identification of cyanamide defects as catalytically relevant sites, *Nat. Commun.* 7 (2016) 12165.
- [37] P. Niu, M. Qiao, Y. Li, L. Huang, T. Zhai, Distinctive defects engineering in graphitic carbon nitride for greatly extended visible light photocatalytic hydrogen evolution, *Nano Energy* 44 (2018) 73–81.
- [38] M. Zhu, Z. Sun, M. Fujitsuka, T. Majima, Z-scheme photocatalytic water splitting on a 2D heterostructure of Black Phosphorus/Bismuth vanadate using visible light, *Angew. Chem. Int. Ed.* 57 (2018) 2160–2164.
- [39] Z. Jin, N. Murakami, T. Tsubota, T. Ohno, Complete oxidation of acetaldehyde over a composite photocatalyst of graphitic carbon nitride and tungsten (VI) oxide under visible-light irradiation, *Appl. Catal. B: Environ.* 150 (2014) 479–485.
- [40] J. Zhang, M. Zhang, R.Q. Sun, X. Wang, A facile band alignment of polymeric carbon nitride semiconductors to construct isotype heterojunctions, *Angew. Chem.* 124 (2012) 10292–10296.
- [41] X. Fan, L. Zhang, M. Wang, W. Huang, Y. Zhou, M. Li, R. Cheng, J. Shi, Constructing carbon-nitride-based copolymers via Schiff base chemistry for visible-light photocatalytic hydrogen evolution, *Appl. Catal. B: Environ.* 182 (2016) 68–73.
- [42] J. Zhang, X. Chen, K. Takanabe, K. Maeda, K. Domen, J.D. Epping, X. Fu, M. Antonietti, X. Wang, Synthesis of a carbon nitride structure for visible-light

- catalysis by copolymerization, *Angew. Chem. Int. Ed.* 49 (2010) 441–444.
- [43] J. Zhang, G. Zhang, X. Chen, S. Lin, L. Möhlmann, G. Dolega, G. Lipner, M. Antonietti, S. Blechert, X. Wang, Co-monomer control of carbon nitride semiconductors to optimize hydrogen evolution with visible light, *Angew. Chem.* 124 (2012) 3237–3241.
- [44] Y. Yu, W. Yan, X. Wang, P. Li, W. Gao, H. Zou, S. Wu, K. Ding, Surface engineering for extremely enhanced charge separation and photocatalytic hydrogen evolution on g-C₃N₄, *Adv. Mater.* 30 (2018) 1705060.
- [45] H. Kasap, C.A. Caputo, B.C. Martindale, R. Godin, V.W.-H. Lau, B.V. Lotsch, J.R. Durrant, E. Reisner, Solar-driven reduction of aqueous protons coupled to selective alcohol oxidation with a carbon nitride–molecular Ni catalyst system, *J. Am. Chem. Soc.* 138 (2016) 9183–9192.
- [46] W. Jiang, Y. Zhu, G. Zhu, Z. Zhang, X. Chen, W. Yao, Three-dimensional photocatalysts with a network structure, *J. Mater. Chem. A* 5 (2017) 5661–5679.
- [47] W. Jiang, W. Luo, J. Wang, M. Zhang, Y. Zhu, Enhancement of catalytic activity and oxidative ability for graphitic carbon nitride, *J. Photoch Photobio C* 28 (2016) 87–115.
- [48] W. Zhou, J. Jia, J. Lu, L. Yang, D. Hou, G. Li, S. Chen, Recent developments of carbon-based electrocatalysts for hydrogen evolution reaction, *Nano Energy* 28 (2016) 29–43.
- [49] S.N. Talapaneni, J.H. Lee, S.H. Je, O. Buyukcakir, Tw. Kwon, K. Polychronopoulou, J.W. Choi, A. Coskun, Chemical blowing approach for ultramicroporous carbon nitride frameworks and their applications in gas and energy storage, *Adv. Funct. Mater.* 27 (2017) 1604658.
- [50] L. Shi, T. Wang, H. Zhang, K. Chang, J. Ye, Electrostatic self-assembly of nanosized carbon nitride nanosheet onto a zirconium metal-organic framework for enhanced photocatalytic CO₂ reduction, *Adv. Funct. Mater.* 25 (2015) 5360–5367.
- [51] J. Sun, J. Zhang, M. Zhang, M. Antonietti, X. Fu, X. Wang, Bioinspired hollow semiconductor nanospheres as photosynthetic nanoparticles, *Nat. Commun.* 3 (2012) 1139.
- [52] Y. Zheng, L. Lin, X. Ye, F. Guo, X. Wang, Helical graphitic carbon nitrides with photocatalytic and optical activities, *Angew. Chem.* 126 (2014) 12120–12124.
- [53] X. Hu, L. Huang, J. Zhang, H. Li, K. Zha, L. Shi, D. Zhang, Facile and template-free fabrication of mesoporous 3D nanosphere-like Mn_xCo_{3-x}O₄ as highly effective catalysts for low temperature SCR of NO_x with NH₃, *J. Mater. Chem. A* 6 (2018) 2952–2963.
- [54] M. Zhang, W. Jiang, D. Liu, J. Wang, Y. Liu, Y. Zhu, Y. Zhu, Photodegradation of phenol via C₃N₄-agar hybrid hydrogel 3D photocatalysts with free separation, *Appl. Catal. B: Environ.* 183 (2016) 263–268.
- [55] Y. Hou, Z. Wen, S. Cui, X. Feng, J. Chen, Strongly coupled ternary hybrid aerogels of n-deficient porous graphitic-C₃N₄ nanosheets/N-doped graphene/NiFe-layered double hydroxide for solar-driven photoelectrochemical water oxidation, *Nano Lett.* 16 (2016) 2268–2277.
- [56] J. Liu, T. An, Z. Chen, Z. Wang, H. Zhou, T. Fan, D. Zhang, M. Antonietti, Carbon nitride nanosheets as visible light photocatalytic initiators and crosslinkers for hydrogels with thermoresponsive turbidity, *J. Mater. Chem. A* 5 (2017) 8933–8938.
- [57] J. Yan, M.T.F. Rodrigues, Z. Song, H. Li, H. Xu, H. Liu, J. Wu, Y. Xu, Y. Song, Y. Liu, Reversible formation of g-C₃N₄ 3D hydrogels through ionic liquid activation: gelation behavior and room-temperature gas-sensing properties, *Adv. Funct. Mater.* 27 (2017) 1700653.
- [58] W. Jiang, W. Luo, R. Zong, W. Yao, Z. Li, Y. Zhu, Polyaniline/carbon nitride nanosheets composite hydrogel: a separation-Free and high-efficient photocatalyst with 3D hierarchical structure, *Small* 12 (2016) 4370–4378.
- [59] H. Ou, P. Yang, L. Lin, M. Anpo, X. Wang, Carbon nitride aerogels for the photo-redox conversion of water, *Angew. Chem.* 56 (2017) 10905–10910.
- [60] G. Zhang, J. Zhang, M. Zhang, X. Wang, Polycondensation of thiourea into carbon nitride semiconductors as visible light photocatalysts, *J. Mater. Chem. C* 22 (2012) 8083–8091.
- [61] G. Zhang, G. Li, Z.A. Lan, L. Lin, A. Savateev, T. Heil, S. Zafeiratos, X. Wang, M. Antonietti, Optimizing optical absorption, exciton dissociation, and charge transfer of a polymeric carbon nitride with ultrahigh solar hydrogen production activity, *Angew. Chem. Int. Ed.* 56 (2017) 13445–13449.
- [62] Q. Cui, J. Xu, X. Wang, L. Li, M. Antonietti, M. Shalom, Phenyl-modified carbon nitride quantum dots with distinct photoluminescence behavior, *Angew. Chem. Int. Ed.* 55 (2016) 3672–3676.
- [63] Z. Song, T. Lin, L. Lin, S. Lin, F. Fu, X. Wang, L. Guo, Invisible security ink based on water-soluble graphitic carbon nitride quantum dots, *Angew. Chem. Int. Ed.* 55 (2016) 2773–2777.
- [64] P. Xia, B. Zhu, J. Yu, S. Cao, M. Jaroniec, Ultra-thin nanosheet assemblies of graphitic carbon nitride for enhanced photocatalytic CO₂ reduction, *J. Mater. Chem. A* 5 (2017) 3230–3238.
- [65] G. Zhang, Z.-A. Lan, L. Lin, S. Lin, X. Wang, Overall water splitting by Pt/g-C₃N₄ photocatalysts without using sacrificial agents, *Chem. Sci.* 7 (2016) 3062–3066.
- [66] Y.S. Jun, E.Z. Lee, X. Wang, W.H. Hong, G.D. Stucky, A. Thomas, From melamine-cyanuric acid supramolecular aggregates to carbon nitride hollow spheres, *Adv. Funct. Mater.* 23 (2013) 3661–3667.
- [67] H. Tong, S. Ouyang, Y. Bi, N. Umezawa, M. Oshikiri, J. Ye, Nano-photocatalytic materials: possibilities and challenges, *Adv. Mater.* 24 (2012) 229–251.
- [68] J. Fang, H. Fan, Z. Zhu, L.B. Kong, L. Ma, “Dyed” graphitic carbon nitride with greatly extended visible-light-responsive range for hydrogen evolution, *J. Catal.* 339 (2016) 93–101.
- [69] Y. Kang, Y. Yang, L.C. Yin, X. Kang, L. Wang, G. Liu, H.M. Cheng, Selective breaking of hydrogen bonds of layered carbon nitride for visible light photocatalysis, *Adv. Mater.* 28 (2016) 6471–6477.
- [70] J. Chen, C.L. Dong, D. Zhao, Y.C. Huang, X. Wang, L. Samad, L. Dang, M. Shearer, S. Shen, L. Guo, Molecular design of polymer heterojunctions for efficient solar-hydrogen conversion, *Adv. Mater.* 29 (2017) 1606198.
- [71] C. Pan, J. Xu, Y. Wang, D. Li, Y. Zhu, Dramatic activity of C₃N₄/BiPO₄ photocatalyst with Core/Shell structure formed by self-assembly, *Adv. Funct. Mater.* 22 (2012) 1518–1524.
- [72] J. Su, L. Guo, N. Bao, C.A. Grimes, Nanostructured WO₃/BiVO₄ heterojunction films for efficient photoelectrochemical water splitting, *Nano Lett.* 11 (2011) 1928–1933.
- [73] Q. Ruan, W. Luo, J. Xie, Y. Wang, X. Liu, Z. Bai, C.J. Carmalt, J. Tang, A nanojunction polymer photoelectrode for efficient charge transport and separation, *Angew. Chem. Int. Ed.* 56 (2017) 8221–8225.
- [74] N. Tian, Y. Zhang, X. Li, K. Xiao, X. Du, F. Dong, G.I. Waterhouse, T. Zhang, H. Huang, Precursor-reforming protocol to 3D mesoporous g-C₃N₄ established by ultrathin self-doped nanosheets for superior hydrogen evolution, *Nano Energy* 38 (2017) 72–81.
- [75] H. Ou, L. Lin, Y. Zheng, P. Yang, Y. Fang, X. Wang, Tri-s-triazine-based crystalline carbon nitride nanosheets for an improved hydrogen evolution, *Adv. Mater.* 29 (2017) 1700008.